

# Feedback driven interactions between dark and luminous matter to explain tight galaxy scaling relations.

Leen Alrawas,<sup>1,2,3\*</sup> Andrea V. Macciò,<sup>1,2</sup> Carlo Cannarozzo,<sup>1,2</sup>

<sup>1</sup>New York University Abu Dhabi, PO Box 129188, Saadiyat Island, Abu Dhabi, UAE

<sup>2</sup>Center for Astrophysics and Space Science (CASS), New York University Abu Dhabi, Saadiyat Island, PO Box 129188, Abu Dhabi, UAE

<sup>3</sup>Department of Physics, New York University, New York NY 10003, USA

Accepted 2026 May 12. Received 2026 April 18; in original form 2025 December 8

## ABSTRACT

The tight empirical correlation linking the stellar disk scale length  $R_d$  to the dark matter scale radius  $r_0$  has been proposed as potential evidence for a fundamental coupling between baryons and dark matter beyond gravity. We re-examine the physical origin of this relation using a sample of 31 galaxies drawn from the NIHAO cosmological hydrodynamical simulations, which include no dark matter–baryon interactions other than gravity and baryonic feedback processes. NIHAO naturally reproduces both the normalization and the small scatter of the observed  $R_d$ – $r_0$  relation at  $z = 0$ , while showing a slightly shallower distribution. By tracking galaxies from  $z = 2$  to  $z = 0$ , we identify three evolutionary classes: systems undergoing disk expansion, contraction, and quasi-static galaxies. Using a Bayesian hierarchical framework, we provide the first evolutionary characterization of the  $R_d$ – $r_0$  relation, tracing how its normalization, slope, and intrinsic scatter evolve across cosmic time, from  $z = 2$  to the present-day Universe. Together with a mild decrease in normalization (by  $\sim 0.07$  dex) and a flattening of the slope from  $\alpha \simeq 1.05$  to  $\alpha \simeq 0.95$ , we find that the intrinsic scatter weakly decreases toward lower redshift, indicating that galaxies tend to evolve along the relation, jointly re-balancing their stellar and dark matter scales. Comparing hydro simulations with their dark matter only counterparts, we can isolate the effect of baryons and baryonic feedback on dark matter evolution. Our results indicate that stellar feedback alone can reshape the central potential and naturally establish the observed coupling between luminous and dark matter, without the need to invoke modifications to the dark sector.

**Key words:** Cosmological simulations – Cold Dark Matter – Scaling relations

## 1 INTRODUCTION

The  $\Lambda$  Cold Dark Matter ( $\Lambda$ CDM) paradigm has emerged as the standard cosmological model, providing a remarkably successful framework for understanding the large-scale structure and evolution of the universe. One of its most compelling achievements lies in its capacity to explain the hierarchical formation of structure, where dark matter halos serve as the gravitational scaffolding for baryonic processes that lead to galaxy formation. Although  $\Lambda$ CDM has proven highly effective on cosmological scales, its success in reproducing the diverse yet tightly correlated properties of galaxies on smaller, galactic scales is a subject of ongoing scrutiny (Del Popolo & Le Delliou 2017; Arora et al. 2023).

Galaxy scaling relations, such as the Tully–Fisher relation (e.g., Tully & Fisher 1977; McGaugh et al. 2000), the stellar-to-halo mass relation (e.g., Brook et al. 2014; Girelli et al. 2020), the velocity-to-brightness relation (e.g., Pizzella et al. 2005; Courteau et al. 2007; Lelli et al. 2013), the radial acceleration relation (e.g., Lelli et al. 2017; Stone & Courteau 2019), and the stellar or gas mass–metallicity relation (e.g., Kewley & Ellison 2008; Ma et al. 2016), represent a subset of key observational constraints on models of galaxy formation and evolution. These relations imply a degree of regularity in

galaxy formation that is not expected given the stochastic nature of baryonic processes such as gas accretion, star formation, and feedback from supernovae and active galactic nuclei (e.g., Cole et al. 1994; Keller et al. 2019). The existence of these correlations has often been perceived as a challenge to  $\Lambda$ CDM-based models (e.g., Navarro 2000; Dutton et al. 2016; Arora et al. 2023), which must simultaneously account for complex, non-linear baryonic physics and the underlying dynamics of dark matter.

In recent years, cosmological hydrodynamical simulations have made impressive progress in reproducing key galaxy scaling relations like the Tully–Fisher relation and the size–mass relation (Crain et al. 2015; Dutton et al. 2017), the mass metallicity relations (Rossi et al. 2017; Nelson et al. 2019; Buck et al. 2021), the stellar mass–halo mass relation (Wang et al. 2015; Pillepich et al. 2018; Macciò et al. 2020b) and many others (see Vogelsberger et al. 2020; Arora et al. 2023, for more details).

Among the many observed galaxy scaling relations, there is one that is of particular interest for dark matter theories and cosmology. This is the observed correlation between the characteristic size of the dark matter halo, typically quantified by the dark matter scale radius  $r_0$ , and the stellar disk scale length  $R_d$  (Donato et al. 2004). This relation provides a direct link between the visible and invisible sides of galaxy formation and might shed some light on the properties of dark matter. Observational studies have revealed a remarkably tight linear

\* E-mail: laa9597@nyu.edu

relationship between these two quantities across a diverse range of galaxy morphologies, encompassing low surface brightness galaxies (Di Paolo et al. 2019), dwarf disk galaxies (Karukes & Salucci 2017), normal spiral galaxies (Donato et al. 2004), and even extending to giant central dominant galaxies, such as M87 (De Laurentis & Salucci 2022).

This pronounced correlation, together with the small scatter, has been interpreted by some authors (e.g. Salucci et al. 2020) as possible evidence for a coupling between the baryonic and dark matter components that may transcend the expectations of purely gravitational interaction (Foot 2014; Nesti et al. 2023).

On the other hand, recent simulations have consistently shown that baryonic processes (e.g., gas accretion and feedback) can alter the DM distribution in galaxies by either contracting or expanding the dark matter halo (Dutton et al. 2007; Abadi et al. 2010; Macciò et al. 2012; Tollet et al. 2016; Chan et al. 2015). This raises the question whether such feedback-driven ‘interactions’ can be the core mechanism to set the  $R_d$ – $r_0$  relation and drive its evolution through cosmic time, without the need to invoke new physics in the dark sector.

In this work, we employ the NIHAO (Numerical Investigation of a Hundred Astrophysical Objects) simulations (Wang et al. 2015) suite to test to what extent numerical simulations are capable of reproducing the observed relations and their scatter, in a model where no additional interactions besides gravity are included.

This paper is organized as follows: Section 2 provides a brief summary of the NIHAO simulations. In Section 3, we present the  $R_d$ – $r_0$  scaling relation derived from observational data alongside the corresponding relation obtained from simulated galaxies. Section 4 discusses two distinct evolutionary pathways through which galaxies may converge toward this relation by redshift  $z = 0$ . The temporal evolution of the scaling relation from  $z = 2$  to  $z = 0$  is examined in Section 5. Finally, the principal findings of this work are summarized in Section 7 together with possible caveats in Section 6.

## 2 THE NIHAO SIMULATIONS

The NIHAO simulations (Wang et al. 2015; Blank et al. 2019) used in this study are based on the GASOLINE2 hydrodynamical code (Wadsley et al. 2017). Simulations include Compton cooling, photoionization, and heating from the ultraviolet background, metal-line cooling, chemical enrichment, star formation, and stellar feedback—including supernovae and early feedback from massive stars (Stinson et al. 2013).

The cosmological parameters of the simulation suite are consistent with the Planck 2016 data release, namely the Hubble parameter is  $H_0 = 67.1 \text{ km s}^{-1} \text{ Mpc}^{-1}$ , with matter density  $\Omega_m = 0.3175$ , dark energy density  $\Omega_\Lambda = 0.6824$ , baryon density  $\Omega_b = 0.0490$ , power spectrum normalization  $\sigma_8 = 0.8344$  and spectral index  $n_s = 0.9624$  (Ade et al. 2016). Each galaxy is resolved with at least 500,000 particles, including DM, gas, and stars. Mass and spatial resolution vary across the sample, ranging from a DM particle mass of  $m_{\text{dm}} = 3.4 \times 10^3 M_\odot$  with gravitational softening  $\epsilon = 100 \text{ pc}$  for dwarf galaxies, up to  $m_{\text{dm}} = 1.4 \times 10^7 M_\odot$  and  $\epsilon = 1.8 \text{ kpc}$  for the most massive systems (see Wang et al. 2015; Blank et al. 2019).

The NIHAO simulations are able to successfully reproduce a wide range of galaxy properties, including the stellar-to-halo mass relation (Wang et al. 2015), the relation between disc gas mass and disc size (Macciò et al. 2016), the Tully–Fisher relation (Dutton et al. 2017), the diversity of galaxy rotation curves (Santos-Santos et al. 2018;

Frosst et al. 2022), and the satellite mass function of the Milky Way and M31 (Buck et al. 2019).

To study the relations between the dark matter scale radius  $r_0$  and the stellar disk radius  $R_d$ , we select 33 galaxies from the NIHAO with stellar and dark matter masses similar to the observed galaxies. Namely, our objects have DM halo with masses in the range  $10^{11} - 10^{12} M_\odot$ , and with stellar masses larger than  $2 \times 10^9 M_\odot$ . Two of the selected systems are found to go through mergers at  $z = 0$ ; for this reason, we exclude these galaxies from the analysis. Thus, our final galaxy sample consists of 31 simulated galaxies.

## 3 REPRODUCING THE $R_d$ – $r_0$ RELATION

In observations, the disc scale parameter ( $R_d$ ) is normally obtained (e.g. Salucci & Burkert 2000; Karukes & Salucci 2017) by fitting the stellar surface density profile with an exponential functional form known as the Freeman disk (Freeman 1970):

$$\mu(R) = \frac{M_D}{2\pi R_d^2} e^{-\frac{R}{R_d}}, \quad (1)$$

where  $M_D$  is the stellar disk mass and  $R_d$  is the stellar disk radius of edge-on spirals.

To recover the dark matter scale radius  $r_0$ , the DM density profiles are assumed to follow a cored profile (which provides a better fit for most disc galaxies (Salucci et al. 2020)), which is usually parametrized with either the Burkert profile (Burkert 1995)

$$\rho_B(r) = \frac{\rho_0}{\left(1 + \frac{r^2}{r_0^2}\right) \left(1 + \frac{r}{r_0}\right)}, \quad (2)$$

or the quasi-isothermal (ISO) profile (Begeman et al. 1991)

$$\rho_{\text{ISO}}(r) = \frac{\rho_0}{\left(1 + \frac{r^2}{r_0^2}\right)}. \quad (3)$$

In both profiles  $\rho_0$  is the dark matter halo central density and  $r_0$  the dark matter halo scale radius.

These two scale radii, describing the distribution of the visible and invisible matter, are connected to very different formation paths, since the dark matter distribution is mostly set at the time of the halo collapse (Bullock et al. 2001; Macciò et al. 2007) while the size of the stellar disc is the final result of several competing phenomena that include, among others, gas cooling, angular momentum conservation, star formation and feedback (e.g. Mo et al. 1998).

Nevertheless, previous authors have reported a tight correlation between  $r_0$  and  $R_d$  with a scatter of around 0.05 (Salucci private communication). In Fig. 1 we compile the most recent results in the literature for this correlation.

Similarly to observations, we computed both the  $r_0$  and  $R_d$  for our set of 31 NIHAO galaxies. The dark matter scale radius  $r_0$  is computed using the isothermal profile (ISO), since this profile provides a better fit to our galaxies than the Burkert profile (see Appendix A for more details).

The disk scale radius  $R_d$  is computed by fitting the projected stellar density, after rotating the galaxy edge-on<sup>1</sup>, with the Freeman profile,

<sup>1</sup> Normally disc scale lengths are better computed for face-on galaxies, but in this work we tried to follow the same procedure as in Nesti et al. (2023) and hence we oriented our galaxies edge-on. There is an offset of about 30% between  $R_d$  values computed with the two different projections, but this does not affect any of the trends discussed in this paper

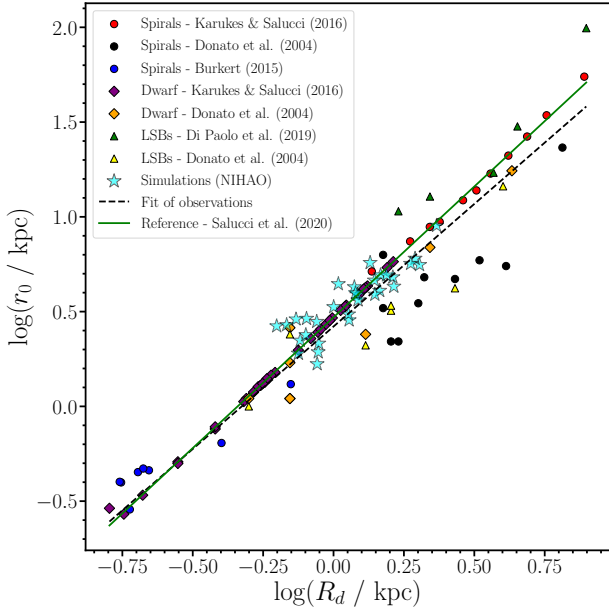


**Figure 1.**  $r_0$  versus  $R_d$  in observed and simulated galaxies. The dashed line is the fit calculated in this work for the observed galaxies, and the green line is the fit reported in Salucci et al. (2020); Nesti et al. (2023) for selected datasets.

following the methodology adopted in Salucci et al. (2020) and Nesti et al. (2023). Two examples of simulated profiles and relative fits are shown in Fig. 2 for the dark matter (upper panel) and the stellar surface density (lower panel) for a galaxy with total mass  $2.41 \times 10^{11} M_\odot$ .

The simulation results in the  $R_d$ – $r_0$  plane are shown in Fig. 1 as (blue) starred symbols. Overall, our simulations are in good agreement with the observations, especially when compared with the fit of all observational data provided in this work (the dashed line). Moreover, NIHAO galaxies also exhibit a small scatter around the relation (the total rms is 0.081 dex), in substantial agreement with observations.

This result is noteworthy, as it demonstrates that a linear relation between the structural parameters of the dark matter halo and the stellar disc can naturally emerge in a  $\Lambda$ CDM Universe, without requiring additional dark matter–baryon interactions beyond gravity.

#### 4 GALAXY EVOLUTIONARY TRACKS IN $R_d$ – $r_0$ PLANE

To study the evolution of a single galaxy in the  $R_d$ – $r_0$  plane, we fit the dark matter and stellar surface density profiles as function of time from  $z = 2$  down to  $z = 0$ , Fig. 3 shows the trajectory of our galaxies as a function of time in this plane<sup>2</sup>.

It is quite interesting that practically all galaxies move *along* the relation (even if in opposite directions), showing a strong correlation in the evolution of these two parameters.

Two distinct evolutionary trends emerge from the analysis of the tracks: a subset of galaxies evolves along the  $R_d$ – $r_0$  relation from left to right, indicating a simultaneous increase in both  $R_d$  and  $r_0$  over cosmic time. Conversely, another group follows the opposite trajectory, migrating from right to left, suggesting a progressive contraction

<sup>2</sup> In NIHAO the name of a galaxy represents its total mass in the low resolution N-body simulation.

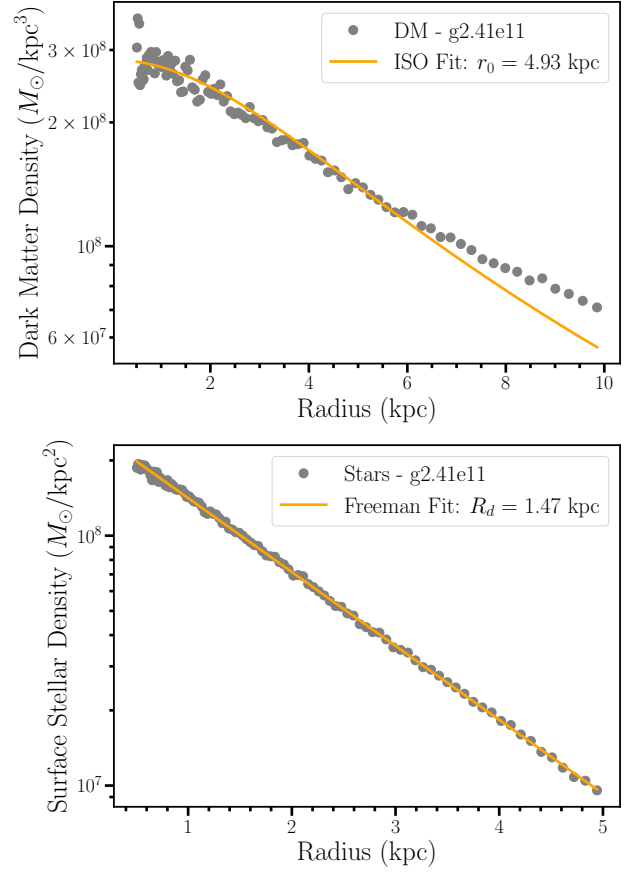


**Figure 2.** The dark matter density profile for a halo of mass  $2.41 \times 10^{11} M_\odot$  fitted to the ISO profile 3, and the surface stellar density profile for the same halo fitted to the Freeman disk 1.

in both scales. Additionally, a small number of galaxies exhibit more stochastic behavior, scattering around a localized region of the plane without adhering to a clear evolutionary path.

To better quantify the evolutionary behavior of galaxies on the  $R_d$ – $r_0$  plane, we classify the sample into three distinct groups based on the direction of their evolution. For each galaxy, we compute the change in both  $R_d$  and  $r_0$  across successive snapshots between  $z = 2$  and  $z = 0$ , using a constant time interval of  $\Delta t = 0.23$  Gyr, uniformly spaced in cosmic time.

Let  $r_0^{(i)}$  and  $R_d^{(i)}$  denote the DM scale radius and disc scale length at time step  $i$ , respectively. The incremental changes between two consecutive steps are given by:

$$\Delta \log r_0^{(i)} = \log r_0^{(i+1)} - \log r_0^{(i)}, \quad \Delta \log R_d^{(i)} = \log R_d^{(i+1)} - \log R_d^{(i)}.$$

The net evolutionary direction of each galaxy is then assessed by averaging over all  $N$  steps:

$$\langle \Delta \log r_0 \rangle = \frac{1}{N} \sum_{i=1}^N \Delta \log r_0^{(i)}, \quad \langle \Delta \log R_d \rangle = \frac{1}{N} \sum_{i=1}^N \Delta \log R_d^{(i)}.$$

Galaxies for which both averages are positive are classified as **"expanding"** (evolving from left to right); for these galaxies, the dark matter inner core and the stellar disk are growing over time. Those with both averages negative are **"contracting"** (evolving from right to left), they have both radii decreasing over time, concentrating more mass in the center of the galaxy. Galaxies with mixed or near-zero values are categorized as **"quasi-static"**, indicating no clear

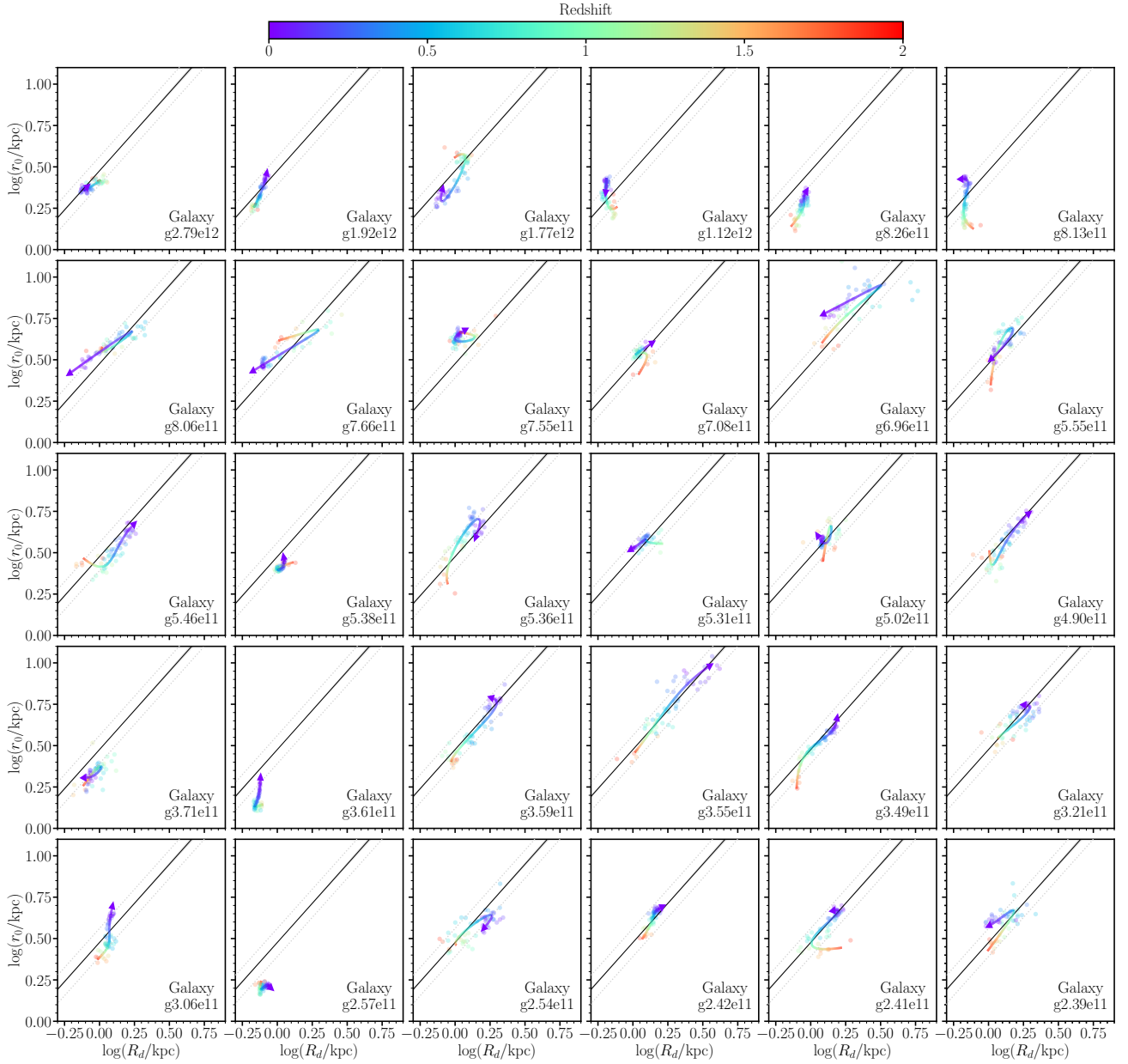


**Figure 3.** Evolution of the  $R_d-r_0$  relation for individual galaxies in the NIHAO sample. Each panel shows the evolutionary track of a single galaxy in the  $\log(R_d)-\log(r_0)$  plane, color-coded by redshift from  $z = 2$  (red) to  $z = 0$  (violet). The trajectories have been smoothed using spline interpolation, and arrows indicate the direction of evolution toward decreasing redshift. The black solid curve represents the median model relation at  $z = 0$ , while the black shaded region marks its  $1\sigma$  credible interval derived from the posterior distribution (see section 5). The light-gray dotted lines indicate the intrinsic scatter of  $\sim 0.085$  dex for the relation at  $z = 0$ . Galaxies are ordered by decreasing stellar mass from the top-left to the bottom-right panels, illustrating how systems of different masses follow distinct evolutionary paths while converging toward the same present-day scaling relation.

*Note* – To smooth the data points for each galaxy, we adopted a cubic B-spline with smoothing factor  $s = 1$ .

directional trend. Fig. 4 presents three representative examples, one for each galaxy family, showing their detailed evolutionary histories. Fig. 5, instead, displays the full sample of galaxies on the  $R_d-r_0$  plane, where each galaxy is shown at its final redshift only.

#### 4.1 The Role of Feedback-driven Interaction

A first indication that baryonic processes play a key role in shaping the evolution on the  $R_d-r_0$  plane comes from comparing hydrodynamical simulations with their dark-matter-only (DMO) counterparts. In

this section, we adopt an alternative definition of  $r_0$  that is better suited to the cuspy density profiles of the DMO runs (Navarro et al. 1997; Macciò et al. 2007). For consistency, the same definition is also applied to the hydrodynamical simulations to enable a direct comparison. We adopt the functional form used by Tollet et al. (2016), given by

$$\rho(r) = \rho_0 \exp \left\{ \lambda \left[ \ln \left( 1 + \frac{r}{r_0} \right) \right]^2 \right\}. \quad (4)$$

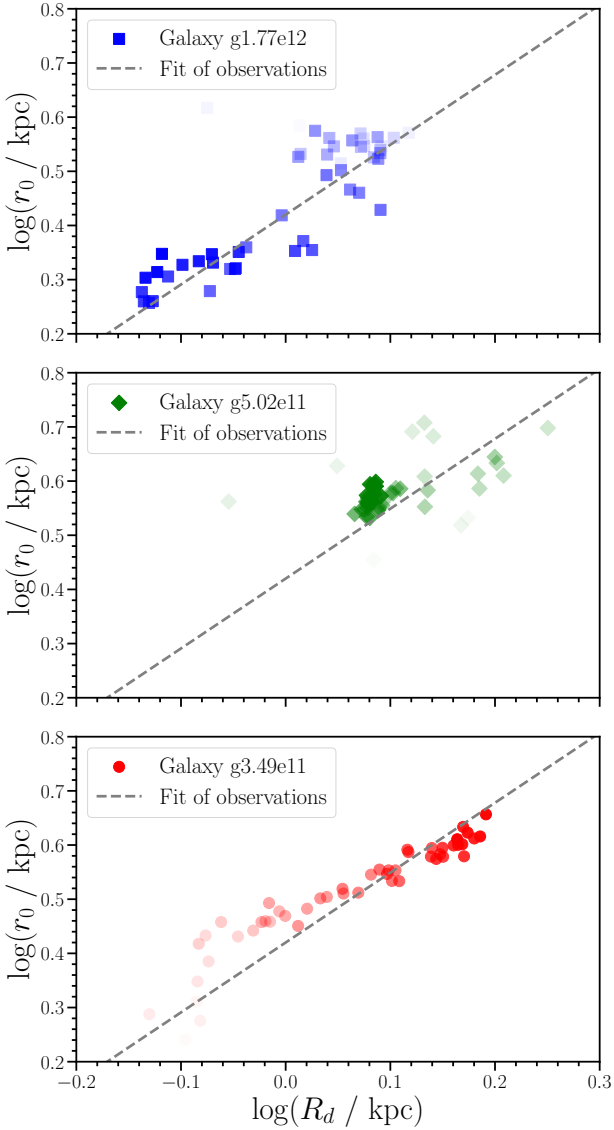


**Figure 4.** The time evolution of three halos on the  $R_d$ – $r_0$  relation from  $z = 2$  to  $z = 0$  where a fainter point indicates an earlier time. The plot shows an expansion of the  $3.49 \times 10^{11} M_\odot$  galaxy and a contraction of the  $1.77 \times 10^{12} M_\odot$  galaxy over time, while the third galaxy of mass  $5.02 \times 10^{11} M_\odot$  doesn’t follow either trend but remains scattered around the same region.

Here,  $\rho_0$  denotes the central density, corresponding to the asymptotic value approached as  $r \rightarrow 0$ . The parameter  $r_0$  defines the characteristic radial scale of the profile; we adopt the fitted value of  $r_0$  as a measure of the core size. The parameter  $\lambda$  controls the curvature of the profile and determines how rapidly the density transitions from the inner region to the outer slope. This functional form is sufficiently flexible to describe both cuspy and cored density profiles.

Fig. 6 shows the relation between the dark matter core scale radius  $r_0$  and halo mass  $M_{\text{DM}}$  for the NIHAO simulations in both Hydro and DMO runs, while Fig. 7 presents the evolutionary tracks of same three representative galaxies shown before.

In the DMO simulations, the evolution follows smooth and monotonic trends, with  $r_0$  varying gradually as halo mass increases through hierarchical assembly. This behavior reflects the purely gravitational evolution of collisionless dark matter. In contrast, the Hydro sim-

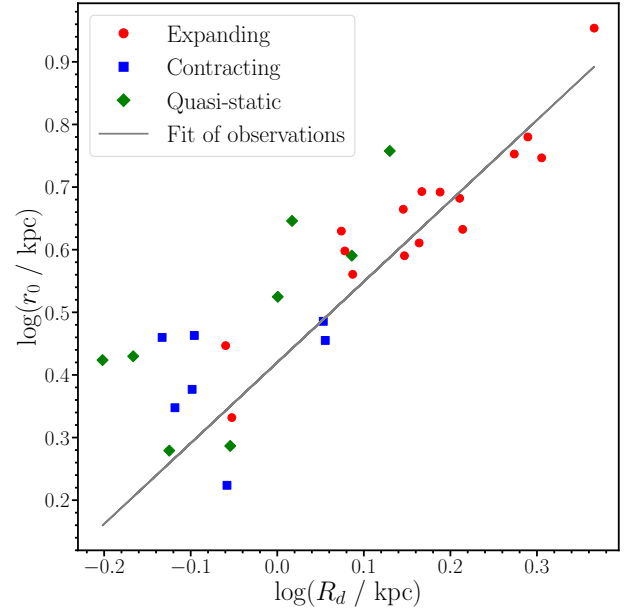


**Figure 5.**  $r_0$  versus  $R_d$  for simulated galaxies at  $z = 0$ , divided into three groups, expanding (red dots), contracting (blue squares), and quasi-static galaxies (green diamonds), according to their evolutionary tracks on the plane. The gray line represents the fit derived in this work for observed galaxies.

ulations exhibit markedly different trajectories and a larger scatter, indicating that baryonic processes significantly alter the inner dark matter structure over time.

For the most massive galaxy (g1.77e12, top row),  $r_0$  initially increases, indicating halo expansion at early times when the system is still assembling and the gravitational potential is relatively shallow. At later times, as the halo grows in mass and a substantial stellar component builds up at the centre, the potential deepens and the dark matter distribution contracts. As a result,  $r_0$  decreases and eventually reaches values smaller than those found in the corresponding DMO run.

The lowest mass galaxy (g3.49e11, low row) shows a markedly different behaviour. In the DMO case,  $r_0$  again remains approximately constant, whereas in the hydrodynamical simulation we observe a clear and sustained expansion of the dark matter distribution. Repeated gas outflows driven by supernova feedback significantly perturb the gravitational potential, forcing the dark matter to respond dynamically by migrating to larger radii (Pontzen & Governato 2012; Tollet et al. 2016). This galaxy a clear indication of feedback-driven baryon–dark matter coupling. By the end of the simulation,  $r_0$  has increased by roughly a factor of 5–10 compared to its initial value.

Finally, the intermediate-mass galaxy (g5.02e11, central row) displays a behaviour in between these two extremes. The hydrodynamical run yields systematically larger values of  $r_0$  than in the DMO case, indicating moderate halo expansion. However, aside from the early phase of halo assembly,  $r_0$  remains approximately constant with time, suggesting that neither strong contraction nor sustained expansion dominates the subsequent evolution.

The NIHAO DMO runs therefore provide a useful baseline for purely gravitational evolution, allowing the deviations seen in the hydrodynamical simulations to be interpreted as the result of baryons an baryonic feedback acting on the dark matter distribution.

To better understand the origin of the different evolutionary behaviours observed on the  $R_d$ – $r_0$  plane, we examined a range of physical

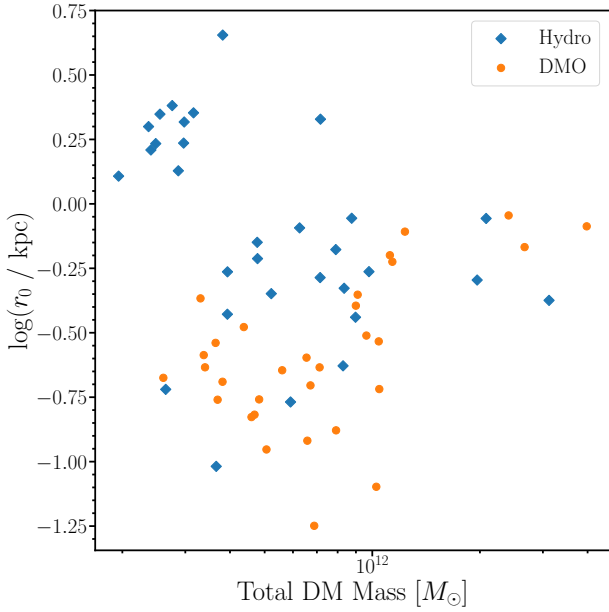


**Figure 6.** The dark matter core radius  $r_0$  versus the total dark matter halo mass of all galaxies at  $z = 0$ .

properties across the three classified groups. Our analysis indicates that stellar and halo mass are key drivers of the evolutionary direction, as shown in Fig. 8. Specifically, galaxies with total masses ( $M_{\text{tot}}$ ) lower than  $10^{11} M_{\odot}$  dominantly exhibit outward evolution, characterized by a monotonic increase in both  $r_0$  and  $R_d$  over time. In contrast, more massive systems tend to follow an inward evolutionary path, with both characteristic radii decreasing across cosmic time. This mass-dependent behavior suggests that shallower potential wells in low-mass halos allow for sustained expansion of baryonic and dark matter distributions, possibly driven by feedback processes (e.g. Pontzen & Governato 2012; Tollet et al. 2016), while at higher masses the additional potential due to the presence of stellar bulge forces the dark matter to contract (e.g. Abadi et al. 2010; Macciò et al. 2020a).

This interpretation is confirmed by the strong correlation of the direction of the movement in the  $R_d$ – $r_0$  plane and the star formation rate (SFR) of the galaxy (as shown in Fig. 9). Galaxies with low or declining SFR tend to show expanding behavior, consistent with a scenario of gradual disc growth and DM core creation (Tollet et al. 2016), while galaxies exhibiting stronger star formation rates (which are usually associated with bulge formation (e.g. Brook et al. 2011)) are more likely to fall into the contracting category.

The ability of baryons to influence and regulate the amount of dark matter in the central region of a galaxy is clearly visible in Fig. 9 where we show the time evolution of the DM mass within a comoving radius of 4 kpc for our three track families. One more time, it is possible to appreciate the *interaction* between visible and invisible matter even in the  $\Lambda$ CDM framework, which does not include any direct interaction mechanism.

Finally, not surprisingly, we find a strong correlation between the inner slope of the dark matter halo profile measured within 2% of the virial radius (Tollet et al. 2016) and the trajectory in the  $R_d$ – $r_0$  plane, as shown in Fig. 9. It is interesting to note that quasi-static galaxies fall in the region where dark matter haloes have retained the

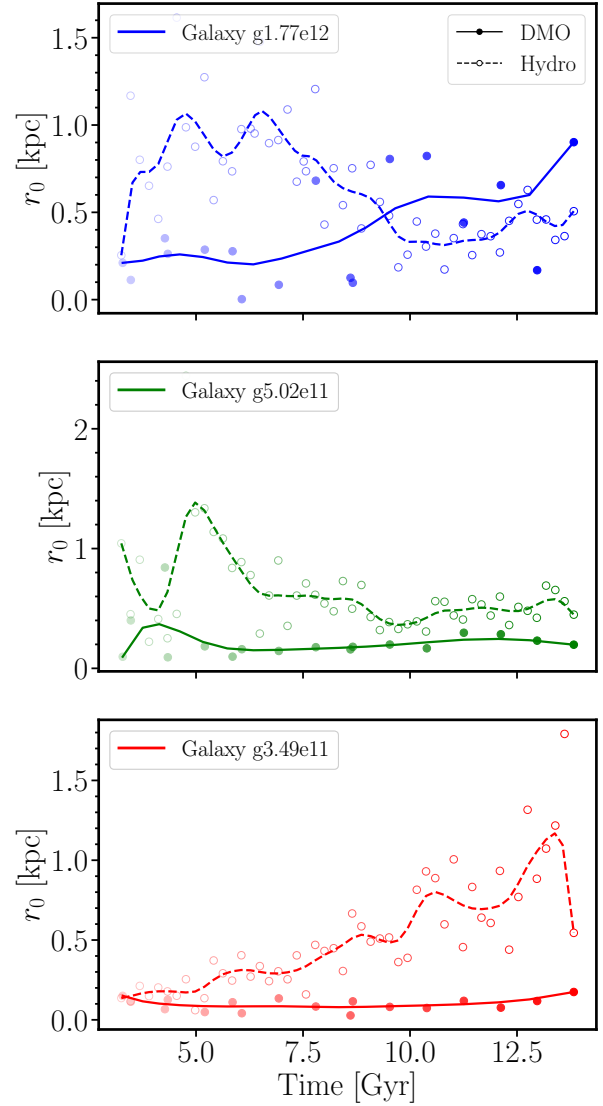


**Figure 7.** The time evolution of three halos on the  $r_0$ –dark matter halo mass plane from  $z = 2$  to  $z = 0$  comparing Hydro and DMO runs. The figure shows three representative cases: a contracting galaxy with halo mass  $1.77 \times 10^{12} M_{\odot}$  (upper panel); a quasi-static galaxy with mass  $5.02 \times 10^{11} M_{\odot}$  (mid panel); an expanding galaxy with mass  $3.49 \times 10^{11} M_{\odot}$  (lower panel).

original NFW-like profile (Navarro 2000), showing no net evolution in their dark matter distribution.

All of the above results seem to strongly suggest a dark-baryonic matter *interaction* via feedback mechanisms. The gentle build-up of the stellar disc (with moderate SFR) is accompanied by stellar feedback, which is able to displace gas from the center of the galaxy in the lower mass haloes in our sample. This gas sloshing generates a time variable potential which induces a non-adiabatic expansion in the DM halo, as initially described in Pontzen & Governato (2012). The net effect is that both the disc and dark matter scale radius grow as a function of time. In massive haloes, vigorous SF in the central region causes the build-up of stellar bulge, which has the effect of reducing the disc scale radius and contracting the dark matter towards the center. The net effect is that both  $R_d$  and  $r_0$  decrease as a function of time (contraction).

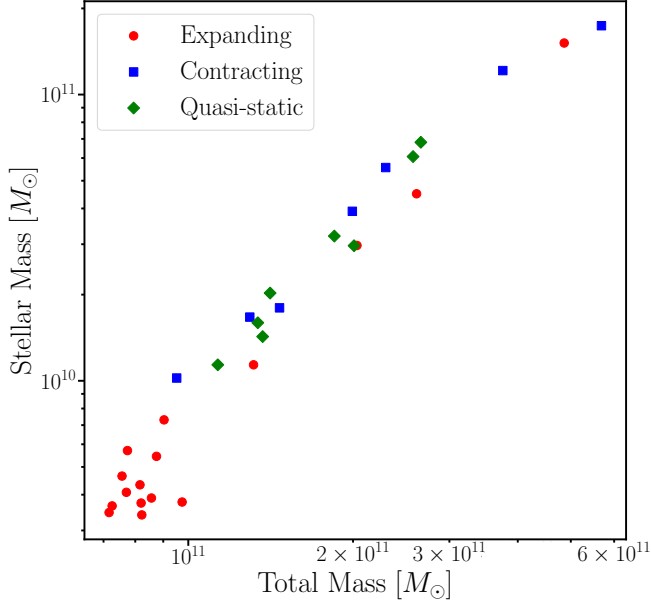


**Figure 8.** The stellar mass versus the total halo mass of all galaxies at  $z = 0$ .

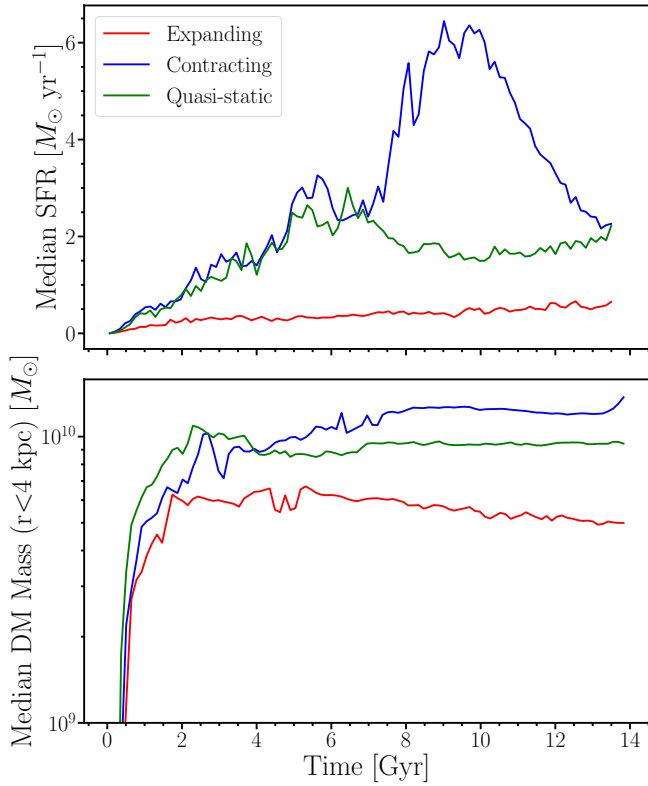


**Figure 9.** The top plot shows the median star formation rate over galaxies in each group according to how the galaxy evolves on the  $R_d$ - $r_0$  relation, while the bottom plot shows the median dark matter mass within 4 kpc for each group.

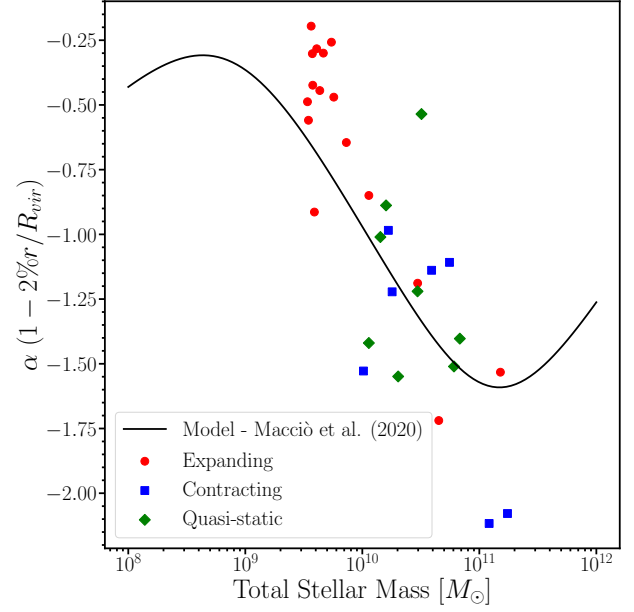


**Figure 10.** Dark matter halo inner density profile slope  $\alpha$  as a function of the stellar mass at redshift  $z = 0$ . The model is retrieved from Macciò et al. (2020a).

Both *expansions* and *contractions* operate to varying degrees in all systems, but it is the dominance of one mechanism over the other that dictates the long-term evolutionary path of the galaxy.

## 5 THE REDSHIFT EVOLUTION OF THE $R_d$ - $r_0$ RELATION

Given the ability of cosmological simulations to trace galaxy evolution across cosmic time, we utilize the simulation outputs at various redshifts to extract the values of  $r_0$  and  $R_d$ , thereby reconstructing the temporal evolution of the  $R_d$ - $r_0$  relation.

### 5.1 The model

As already noted in section 4, galaxies evolve by gradually changing their physical properties, including both  $r_0$  and  $R_d$ , eventually approaching the linear regime observed in the present-day Universe. We now aim to provide a quantitative description of how the global relation between  $r_0$  and  $R_d$  evolves continuously throughout cosmic history, analyzing how its intrinsic scatter varies as well. For this scope, similarly to the approach adopted in Waterval et al. (2025) (see also Cannarozzo et al. 2020), we make use of Bayesian hierarchical modeling to reconstruct the evolution of the relation between  $r_0$  and  $R_d$ .

We adopt a single power-law evolutionary model in which the quantity  $\log r_0$  depends linearly on  $\log R_d$  with coefficients evolving with redshift. The relation is expressed as

$$\mu(z, \log R_d) = \log r_0(z) + \alpha(z) \log R_d, \quad (5)$$

with

$$\log r_0(z) = \log r_{0,0} + \log r_{0,z} z, \quad (6)$$

and

$$\alpha(z) = \alpha_0 + \alpha_z z. \quad (7)$$

Furthermore, to account for intrinsic scatter and any possible evolution of that, we assume the data follow a Gaussian distribution centered on  $\mu$  with variance  $\sigma^2(z)$ , i.e.

$$\mathcal{P}(\log R_0 | \Theta) = \mathcal{N}(\mu(z, \log R_d), \sigma^2(z)), \quad (8)$$

where  $\Theta = \{\log r_{0,0}; \log r_{0,z}; \alpha_0; \alpha_z; \sigma_0; \sigma_z\}$  is the set of parameters to describe the evolutionary single power-law relation. The standard deviation in Equation 8 is modeled as

$$\sigma(z) = \sigma_0 + \sigma_z z. \quad (9)$$

The corresponding log-likelihood is

$$\ln \mathcal{L} = -\frac{1}{2} \sum_i \left( \frac{(\log r_{0,i} - \mu_i)^2}{\sigma_i^2} + \ln(2\pi\sigma_i^2) \right). \quad (10)$$

where the index  $i$  runs over the individual NIHAO galaxies.

Further details about the parameters adopted and their prior ranges, as well as their posterior, are presented in Appendix B.

## 5.2 The results

We performed the parameter inference using the *Nested Sampling* algorithm, as implemented in the *DYNESTY* package (Speagle 2020; Koposov et al. 2023). The sampling setup and the adopted priors for the model hyperparameters are described in detail in Appendix B. The best-fitting relations at different redshifts are shown in Figure 11, color-coded by  $z$ . The model predicts a gradual steepening of the  $\log r_0$ – $\log R_d$  relation toward higher redshift, while simultaneously reproducing the progressive tightening of its intrinsic scatter at later times. The median values and 68% credible intervals of all hyperparameters are listed in Table 1.

At  $z = 0$ , our best-fit relation (violet curve in Figure 11) lies slightly below the local calibration by Nesti et al. (2023), shown as a gray dashed line. This offset originates from differences in the inferred slopes: while Nesti et al. (2023) report  $\alpha = 1.38 \pm 0.15$  and  $\log r_{0,0} = 0.47 \pm 0.03$ , our posterior analysis yields  $\alpha(z = 0) \simeq 0.95$  and  $\log r_{0,0}(z = 0) \simeq 0.48$  (see Figure 12). The two results are therefore consistent in normalization but differ significantly in slope, implying a shallower dependence of  $\log r_0$  on  $\log R_d$  in our model. Quantitatively, our relation lies  $\sim +0.08$  dex above the Nesti et al. (2023) relation at  $\log R_d = -0.2$  kpc, becomes nearly coincident around  $\log R_d \simeq 0$ , and falls progressively below it by  $-0.08$  and  $-0.15$  dex at  $\log R_d = 0.2$  and  $0.4$ , respectively. This systematic deviation, clearly visible in Figure 11, reflects the flatter slope inferred from our nested-sampling posterior, despite the overall agreement in normalization.

We find that, from  $z = 2$  to  $z = 0$ , the normalization decreases by  $\sim 0.07$  dex, while the slope flattens from  $\alpha \simeq 1.05$  to  $\alpha \simeq 0.95$ , indicating a mild but coherent evolution toward shallower trends at later times. This behaviour reflects the gradual structural coevolution of the stellar and dark matter components, which become more tightly coupled as the Universe ages.

The inset panel in Figure 11 illustrates the weak redshift evolution of the intrinsic scatter  $\sigma(z)$ , which increases from  $\sigma \simeq 0.086$  dex at  $z = 0$  to  $\sigma \simeq 0.094$  dex at  $z = 2$ . This slight broadening indicates that, although the  $R_d$ – $r_0$  relation is already tight at late times, it becomes marginally more dispersed at earlier epochs. Such an evolution suggests that the structural diversity of galaxies was larger when disks were still assembling and baryon–dark matter coupling was more dynamically variable. At high redshift, stochastic processes—such as bursty star formation, feedback-driven potential fluctuations, and irregular accretion histories—likely contributed to this increased dispersion. By contrast, toward  $z = 0$ , the reduced scatter reflects the

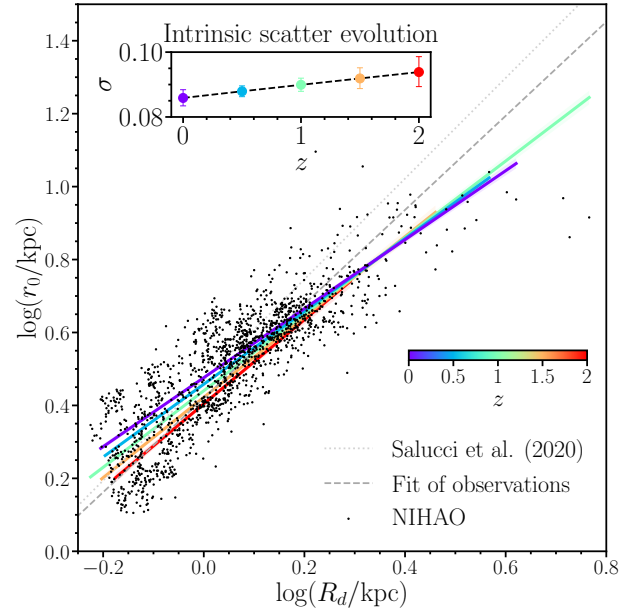


**Figure 11.** Cosmic evolution of the  $R_d$ – $r_0$  relation from  $z = 2$  to  $z = 0$ . The solid colored lines show the median relation at different redshifts ( $z = 0, 0.5, 1, 1.5, 2$ ). The shaded bands represent the  $1\sigma$  credible regions from the Bayesian hierarchical model. The black points correspond to all NIHAO galaxies across all available snapshots between  $z = 2$  and  $z = 0$ . The light gray dotted line shows the relation from Salucci et al. (2020), while the dark gray dashed line represents the linear fit to the full compilation of observational data presented in Figure 1. The inset panel illustrates the evolution of the intrinsic scatter (black dashed line), with the colored points and error bars indicating the median and 16th–84th percentile ranges of the posterior distributions at each redshift.

secular stabilization of disks and the emergence of a self-regulated equilibrium between stellar and dark matter scales.

In summary, the evolution of the  $R_d$ – $r_0$  relation across the redshift range  $0 \lesssim z \lesssim 2$  can be approximately described as

$$\log \left( \frac{r_0}{\text{kpc}} \right) \simeq (0.476 - 0.036z) + (0.946 + 0.104z) \log R_d, \quad (11)$$

based on the median posterior values of the hyperparameters. The weak evolution of the intrinsic scatter is captured by

$$\log \left( \frac{\sigma}{\text{dex}} \right) \simeq 0.086 + 0.004z, \quad (12)$$

indicating a mild increase of scatter with redshift, consistent with the trend shown in the inset of Figure 11.

In Figure 13, we show an interpretative cartoon that illustrates how galaxies follow different evolutionary pathways in the relation between the disk scale length and the DM scale radius, before all converging onto the observed tight relation at  $z = 0$ . Expanding systems (red) increase both  $R_d$  and  $r_0$  with time, while contracting systems (blue) decrease both quantities, and “quasi-static” galaxies (green) remain relatively stable, only oscillating around the final trend. These structural differences are closely connected to their star formation histories: expanding galaxies maintain a low and flat star formation rate, contracting galaxies sustain a high and extended star formation activity, and “quasi-static” galaxies show a pronounced early peak followed by a steady decline. The inset with concentric circles further emphasizes how the two characteristic radii evolve in each category,

**Table 1.** Median values and 68% credible intervals of the posterior distributions for the hyperparameters of the evolutionary model.

Hyperparameter	Inferred value
$\log r_{0,0}$	$0.476^{+0.004}_{-0.004}$
$\log r_{0,z}$	$-0.036^{+0.005}_{-0.005}$
$\alpha_0$	$0.946^{+0.024}_{-0.023}$
$\alpha_z$	$0.104^{+0.037}_{-0.037}$
$\sigma_0$	$0.086^{+0.003}_{-0.002}$
$\sigma_z$	$0.004^{+0.003}_{-0.003}$

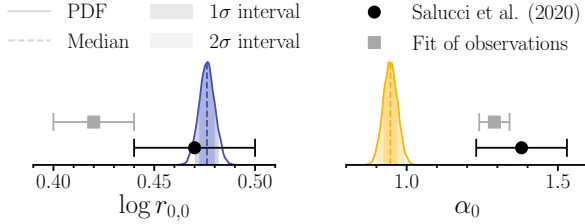


**Figure 12.** Posterior probability density functions (PDFs) for the normalization ( $\log r_{0,0}$ , left) and slope ( $\alpha_0$ , right) of the  $R_d-r_0$  relation at  $z = 0$ . The colored curves show the marginalized PDFs, with dashed vertical lines marking the median values and shaded regions indicating the  $1\sigma$  (dark) and  $2\sigma$  (light) credible intervals. Black circles and horizontal error bars denote the observational estimates from Salucci et al. (2020), while gray squares represent the best-fit values obtained from the linear fit to the full set of observational data compiled from the literature, as described in Figure 1. The comparison highlights the close agreement between the simulated posterior distributions and the empirical measurements at  $z = 0$ .

highlighting the distinct evolutionary tracks that nonetheless collapse onto the same relation at the present-day Universe.

## 6 CAVEATS

- *Intrinsic differences between observations and simulations.* While both datasets aim to describe the same physical systems, simulations rely on sub-grid physics and resolution limits (Hopkins et al. 2018), whereas observations are constrained by instrumental sensitivity, projection effects, and selection biases (Conselice 2014). These intrinsic differences must be acknowledged when drawing one-to-one comparisons (Somerville & Davé 2015; Naab & Ostriker 2017).

- *Different methods to derive physical quantities.* Stellar masses or radii are often obtained using distinct techniques in observations (e.g., photometric or spectroscopic fitting) and simulations (e.g., particle summation within a given metric) (Torrey et al. 2015). Such methodological inconsistencies can lead to systematic offsets in derived relations.

- *Choice of radial profiles and metrics.* Observational studies typically measure quantities within projected metrics (e.g.,  $R_e$ , or fixed physical sizes), while simulations can access full 3D profiles (Schaye et al. 2015). The choice of metric or profile definition strongly impacts global quantities and scaling relations (Pillepich et al. 2018; Rodriguez-Gomez et al. 2019). Moreover, the adopted photometric band also affects measured galaxy sizes: multi-band analyses show

systematic differences of effective radius (e.g., Vulcani et al. 2014; Kennedy et al. 2015), and mock radiative-transfer predictions from cosmological simulations (e.g., TNG50–SKIRT) reveal size variations of up to  $\sim 50\%$  across different bands (Baes et al. 2024). We emphasize here that, in our analysis, we did not perform mock observations of the simulated galaxies to produce wavelength-dependent maps directly comparable to observations, as such an analysis lies beyond the scope of this work.

- *Impact of resolution and numerical effects.* Finite spatial and mass resolution in simulations can affect the internal structure of galaxies, especially at low masses, influencing size, morphology, and kinematic measurements (Hopkins et al. 2018; Buck et al. 2020). Resolution convergence tests are essential for robust interpretations.

- *Uncertainties in stellar population modeling.* Translating between observed light and simulated stellar mass requires assumptions about IMF, stellar evolution, and dust attenuation. Differences in these assumptions can introduce additional scatter and bias (MacArthur et al. 2003; Conroy et al. 2009).

## 7 CONCLUSIONS

Galaxy scaling relations are a natural testbed for any models aiming to reproduce the formation and evolution of galaxies through cosmic time. In this work, we focus our attention on the observed tight correlations between the scale radius of the dark matter distribution, usually obtained via the study of rotation curves (Di Paolo et al. 2019) and the exponential scale radius of the stellar disc (e.g. Begeman et al. 1991; Karukes & Salucci 2017).

This tight relation between the distribution of the invisible and visible matter might suggest a possible interaction in the dark sector beyond gravity (e.g. Nesti et al. 2023); it is then important to check to what extent such a relation can be reproduced in the standard  $\Lambda$ CDM model, which does not include any additional interaction.

We analyzed 31 high-resolution simulated galaxies from the NI-HAO suite (Wang et al. 2015) in a mass range similar to the observed one. Our results show that it is indeed possible to reproduce a very tight relation with very low scatter (less than 0.09 dex) in a model where the dark and luminous matter only interact via gravity.

The correlation between the stellar and dark matter distributions is already in place at  $z = 2$ , even though with a slightly larger scatter than at  $z = 0$ . Subsequently, galaxies tend to move *along* the relation by either expanding or contracting the scale radius of both the distributions. To quantitatively trace how the  $R_d-r_0$  relation evolves across cosmic time, we rely on a Bayesian hierarchical approach. The mild decrease in normalization and the progressive flattening of the slope toward lower redshift indicate that the structural coupling between stellar and dark matter components becomes tighter with time. Galaxies appear to evolve along the  $R_d-r_0$  relation, maintaining a self-regulated balance between their baryonic and dark matter components as the Universe ages. Furthermore, we find that the intrinsic scatter weakly decreases toward lower redshift, indicating that galaxies, regardless of their individual evolutionary pathways, tend to evolve coherently along the relation, re-balancing their stellar and dark matter scales.

Galaxies with vigorous star formation histories tend to form a larger bulge, smaller disc, and contract (almost adiabatically) the DM distribution (Blumenthal et al. 1986; Abadi et al. 2010), moving then right to left and top to bottom in the  $R_d-r_0$  plane. Galaxies with a more gentle star formation history then to form larger discs, and expand the DM halo via SuperNovae feedback (Pontzen & Governato

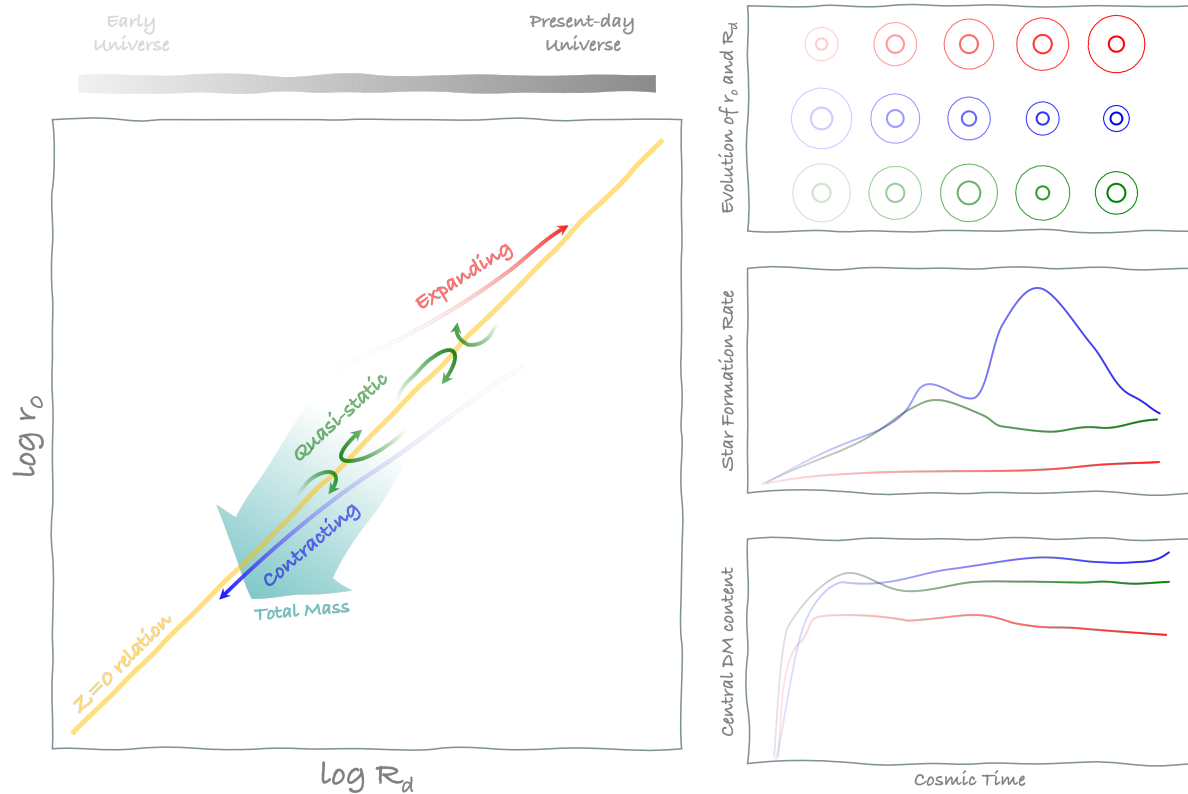


**Figure 13.** Cartoon representation of the evolutionary pathways of galaxies in the  $R_d$ – $r_0$  plane and related quantities. The left panel illustrates the average evolutionary trajectories of “expanding” (red), “contracting” (blue), and “quasi-static” (green) galaxies, which follow distinct pathways but converge toward the same tight  $z = 0$  relation (orange line). The large teal arrow indicates the overall trend with galaxy mass at  $z = 0$ . The top-right panel shows the evolution of  $r_0$  (thick circle) and  $R_d$  (thin circle), the middle panel the star formation rate (SFR), and the bottom panel the inner dark matter content. Color gradients along each track, curve, and on the concentric circles (solid for stellar disks, dotted for dark matter scale radius) trace cosmic time, with more intense hues marking more recent epochs. These panels illustrate how structural and baryonic properties coevolve along different evolutionary channels while maintaining a coherent link between disk growth, central mass buildup, and global size evolution.

2012; Macciò et al. 2012; Tollet et al. 2016) moving from left to right and bottom to top in the  $R_d$ – $r_0$  plane.

Our results indicate that *star formation and feedback-driven baryonic processes* can account for the emergence of a tight correlation between the stellar disk exponential radius  $R_d$  and the dark matter scale radius  $r_0$ , without requiring interactions beyond gravity as a natural outcome of galaxy formation.

In sum, the  $\Lambda$ CDM model—despite its minimal assumptions regarding dark matter interactions—continues to provide a compelling and predictive framework for understanding the structural regularities of galaxies.

## ACKNOWLEDGEMENTS

The authors thank Paolo Salucci for his valuable insights during the early stages of this work. We also thank Stéphane Courteau for his valuable discussions and constructive feedback, which helped improve this work. This material is based on work supported by Tamkeen under the NYU Abu Dhabi Research Institute grant CASS.

## DATA AVAILABILITY

The data underlying this article will be shared on reasonable request to the corresponding author.

## REFERENCES

- Abadi M. G., Navarro J. F., Fardal M., Babul A., Steinmetz M., 2010, *MNRAS*, **407**, 435
- Ade P. A., et al., 2016, *Astronomy & Astrophysics*, **594**, A13
- Arora N., Courteau S., Stone C., Macciò A. V., 2023, *Monthly Notices of the Royal Astronomical Society*, **522**, 1208
- Baes M., Camps P., Rodriguez-Gomez V., Nelson D., Pillepich A., et al., 2024, *Astronomy & Astrophysics*, **690**, A40
- Begeman K., Broeils A., Sanders R., 1991, *Monthly Notices of the Royal Astronomical Society*, **249**, 523
- Blank M., Macciò A. V., Dutton A. A., Obreja A., 2019, *Monthly Notices of the Royal Astronomical Society*, **487**, 5476
- Blumenthal G. R., Faber S. M., Flores R., Primack J. R., 1986, *ApJ*, **301**, 27
- Brook C. B., et al., 2011, *MNRAS*, **415**, 1051
- Brook C., Di Cintio A., Knebe A., Gottlöber S., Hoffman Y., Yepes G., Garrison-Kimmel S., 2014, *The Astrophysical Journal Letters*, **784**, L14
- Buck T., Macciò A. V., Dutton A. A., Obreja A., Frings J., 2019, *Monthly Notices of the Royal Astronomical Society*, **483**, 1314
- Buck T., Obreja A., Macciò A. V., Minchev I., Dutton A. A., Ostriker J. P., 2020, *Monthly Notices of the Royal Astronomical Society*, **491**, 3461
- Buck T., Rybizki J., Buder S., Obreja A., Macciò A. V., Pfrommer C., Steinmetz M., Ness M., 2021, *MNRAS*, **508**, 3365
- Bullock J. S., Kolatt T. S., Sigad Y., Somerville R. S., Kravtsov A. V., Klypin A. A., Primack J. R., Dekel A., 2001, *MNRAS*, **321**, 559
- Burkert A., 1995, *The Astrophysical Journal*, **447**, L25
- Cannarozzo C., Sonnenfeld A., Nipoti C., 2020, *MNRAS*, **498**, 1101
- Chan T. K., Kereš D., Oñorbe J., Hopkins P. F., Muratov A. L., Faucher-

- Giguère C.-A., Quataert E., 2015, *MNRAS*, **454**, 2981
- Cole S., Aragon-Salamanca A., Frenk C. S., Navarro J. F., Zepf S. E., 1994, *Monthly Notices of the Royal Astronomical Society*, **271**, 781
- Conroy C., Gunn J. E., White M., 2009, *The Astrophysical Journal*, **699**, 486
- Conselice C. J., 2014, *Annual Review of Astronomy and Astrophysics*, **52**, 291
- Courteau S., McDonald M., Widrow L. M., Holtzman J., 2007, *The Astrophysical Journal*, **655**, L21
- Crain R. A., et al., 2015, *Monthly Notices of the Royal Astronomical Society*, **450**, 1937–1961
- De Laurentis M., Salucci P., 2022, *The Astrophysical Journal*, **929**, 17
- Del Popolo A., Le Delliou M., 2017, *Galaxies*, **5**, 17
- Di Paolo C., Salucci P., Erkert A., 2019, *Monthly Notices of the Royal Astronomical Society*, **490**, 5451
- Donato F., Gentile G., Salucci P., 2004, *Monthly Notices of the Royal Astronomical Society*, **353**, L17
- Dutton A. A., van den Bosch F. C., Dekel A., Courteau S., 2007, *The Astrophysical Journal*, **654**, 27
- Dutton A. A., Macciò A. V., Frings J., Wang L., Stinson G. S., Penzo C., Kang X., 2016, *Monthly Notices of the Royal Astronomical Society: Letters*, **457**, L74
- Dutton A. A., et al., 2017, *Monthly Notices of the Royal Astronomical Society*, **467**, 4937
- Foot R., 2014, *Journal of Cosmology and Astroparticle Physics*, **2014**, 047
- Freeman K. C., 1970, *Astrophysical Journal*, vol. 160, p. 811, 160, 811
- Frosst M., Courteau S., Arora N., Stone C., Macciò A. V., Blank M., 2022, *Monthly Notices of the Royal Astronomical Society*, **514**, 3510
- Girelli G., Pozzetti L., Bolzonella M., Giocoli C., Marulli F., Baldi M., 2020, *Astronomy & Astrophysics*, **634**, A135
- Hopkins P. F., et al., 2018, *Monthly Notices of the Royal Astronomical Society*, **480**, 800
- Karukes E. V., Salucci P., 2017, *Monthly Notices of the Royal Astronomical Society*, **465**, 4703
- Keller B., Wadsley J., Wang L., Kruijssen J. D., 2019, *Monthly Notices of the Royal Astronomical Society*, **482**, 2244
- Kennedy R., Bamford S. P., Häußler B., Brough S., Driver S. P., et al., 2015, *Monthly Notices of the Royal Astronomical Society*, **454**, 806
- Kewley L. J., Ellison S. L., 2008, *The Astrophysical Journal*, **681**, 1183
- Koposov S., et al., 2023, [joshspeagle/dynesty: v2.1.3, doi:10.5281/zenodo.8408702](https://doi.org/10.5281/zenodo.8408702)
- Lelli F., Fraternali F., Verheijen M., 2013, *Monthly Notices of the Royal Astronomical Society: Letters*, **433**, L30
- Lelli F., McGaugh S. S., Schombert J. M., Pawlowski M. S., 2017, *The Astrophysical Journal*, **836**, 152
- Ma X., Hopkins P. F., Faucher-Giguère C.-A., Zolman N., Muratov A. L., Kereš D., Quataert E., 2016, *Monthly Notices of the Royal Astronomical Society*, **456**, 2140
- MacArthur L. A., Courteau S., Holtzman J. A., 2003, *The Astrophysical Journal*, **582**, 689
- Macciò A. V., Dutton A. A., Van Den Bosch F. C., Moore B., Potter D., Stadel J., 2007, *Monthly Notices of the Royal Astronomical Society*, **378**, 55
- Macciò A. V., Stinson G., Brook C. B., Wadsley J., Couchman H. M. P., Shen S., Gibson B. K., Quinn T., 2012, *ApJ*, **744**, L9
- Macciò A. V., Udrescu S. M., Dutton A. A., Obreja A., Wang L., Stinson G. R., Kang X., 2016, *Monthly Notices of the Royal Astronomical Society: Letters*, **463**, L69
- Macciò A. V., Crespi S., Blank M., Kang X., 2020a, *Monthly Notices of the Royal Astronomical Society: Letters*, **495**, L46
- Macciò A. V., Courteau S., Ouellette N. N.-Q., Dutton A. A., 2020b, *MNRAS*, **496**, L101
- McGaugh S. S., Schombert J. M., Bothun G. D., De Blok W., 2000, *The Astrophysical Journal*, **533**, L99
- Mo H. J., Mao S., White S., 1998, *Monthly Notices of the Royal Astronomical Society*, **295**, 319
- Naab T., Ostriker J. P., 2017, *Annual review of astronomy and astrophysics*, **55**, 59
- Navarro J. F., 2000, arXiv preprint astro-ph/0012334
- Navarro J. F., Frenk C. S., White S. D. M., 1997, *ApJ*, **490**, 493
- Nelson D., Springel V., Marinacci F., Torrey P., Vogelsberger M., Pillepich A., . . . 2019, *Computational Astrophysics and Cosmology*, **6**
- Nesti F., Salucci P., Turini N., 2023, *Astronomy*, **2**, 90
- Pillepich A., et al., 2018, *Monthly Notices of the Royal Astronomical Society*, **475**, 648
- Pizzella A., Corsini E., Dalla Bontà E., Sarzi M., Coccato L., Bertola F., 2005, *The Astrophysical Journal*, **631**, 785
- Pontzen A., Governato F., 2012, *MNRAS*, **421**, 3464
- Rodriguez-Gomez V., et al., 2019, *Monthly Notices of the Royal Astronomical Society*, **483**, 4140
- Rossi M. E. D., Bower R. G., Font A. S., Schaye J., Theuns T., 2017, *Monthly Notices of the Royal Astronomical Society*, **472**, 3354
- Salucci P., Burkert A., 2000, *The Astrophysical Journal*, **537**, L9
- Salucci P., Turini N., Di Paolo C., 2020, *Universe*, **6**, 118
- Santos-Santos I. M., Di Cintio A., Brook C. B., Macciò A., Dutton A., Domínguez-Tenreiro R., 2018, *Monthly Notices of the Royal Astronomical Society*, **473**, 4392
- Schaye J., et al., 2015, *Monthly Notices of the Royal Astronomical Society*, **446**, 521
- Somerville R. S., Davé R., 2015, *Annual Review of Astronomy and Astrophysics*, **53**, 51
- Speagle J. S., 2020, *MNRAS*, **493**, 3132
- Stinson G., Brook C., Macciò A., Wadsley J., Quinn T., Couchman H., 2013, *Monthly Notices of the Royal Astronomical Society*, **428**, 129
- Stone C., Courteau S., 2019, *The Astrophysical Journal*, **882**, 6
- Tollet E., et al., 2016, *Monthly Notices of the Royal Astronomical Society*, **456**, 3542
- Torrey P., et al., 2015, *Monthly Notices of the Royal Astronomical Society*, **447**, 2753
- Tully R. B., Fisher J. R., 1977, *Astronomy and Astrophysics*, vol. 54, no. 3, Feb. 1977, p. 661-673., **54**, 661
- Vogelsberger M., Marinacci F., Torrey P., et al. 2020, *Nature Reviews Physics*, **2**, 42–66
- Vulcani B., Bamford S. P., Häußler B., Vika M., Brough S., et al., 2014, *The Astrophysical Journal*, **788**, 57
- Wadsley J. W., Keller B. W., Quinn T. R., 2017, *Monthly Notices of the Royal Astronomical Society*, **471**, 2357
- Wang L., Dutton A. A., Stinson G. S., Macciò A. V., Penzo C., Kang X., Keller B. W., Wadsley J., 2015, *Monthly Notices of the Royal Astronomical Society*, **454**, 83
- Waterval S., Cannarozzo C., Macciò A. V., 2025, *MNRAS*, **537**, 2726

## APPENDIX A: BURKERT VERSUS ISO FITS

We fit the dark matter density profiles of the galaxies using both the isothermal (ISO) and Burkert models, and computed the corresponding  $\chi^2$  values for each fit. On average, the Burkert profile yields  $\chi^2$  values approximately 48% higher than those of the ISO model (Fig. A1), indicating a systematically poorer fit. The fitting procedure was restricted to the central dark matter region, typically spanning 10–50 kpc, depending on the size of each galaxy. Notably, the Burkert profile begins to deviate significantly from the simulated density distribution beyond roughly three-quarters of this radial range. This divergence arises because the Burkert profile declines more steeply with radius ( $\propto r^{-3}$ ) compared to the isothermal profile ( $\propto r^{-2}$ ).

## APPENDIX B: THE BAYESIAN HIERARCHICAL FRAMEWORK

To infer the redshift evolution of the  $R_d-r_0$  relation and its intrinsic scatter, we employ a Bayesian hierarchical framework. This approach allows us to describe the global behaviour of the simulated galaxy population through a set of hyperparameters that govern the evolution of the relation across cosmic time.

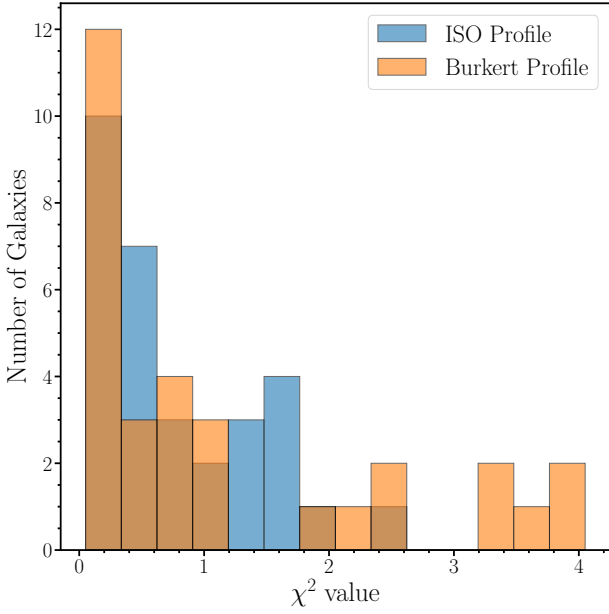


**Figure A1.** Histograms of the  $\chi^2$  values for dark matter fits using the Burkert profile versus the fits using the ISO profile. The Burkert profile shows higher values on average.

Each galaxy in the NIHAO sample is characterized by three physical quantities:

- the disc scale radius,  $R_d$ ;
- the DM scale radius,  $r_0$ ;
- the redshift,  $z$ .

We collect these quantities into a vector of parameters  $\Phi = \{R_d, r_0, z\}$ . Under the hierarchical assumption, the galaxies are considered realizations drawn from a common parent distribution described by a set of hyperparameters  $\Theta$ :

$$\mathcal{P}(\Phi) = \mathcal{P}(\Phi | \Theta). \quad (\text{B1})$$

According to Bayes' theorem, the posterior probability of the hyperparameters given the data,  $\mathcal{D}$ , is

$$\mathcal{P}(\Theta | \mathcal{D}) = \frac{\mathcal{P}(\mathcal{D} | \Theta) \mathcal{P}(\Theta)}{\mathcal{P}(\mathcal{D})}, \quad (\text{B2})$$

where  $\mathcal{P}(\mathcal{D} | \Theta)$  is the *likelihood*,  $\mathcal{P}(\Theta)$  represents the *prior* distributions of the hyperparameters, and  $\mathcal{P}(\mathcal{D})$  is the *Bayesian evidence* ensuring proper normalization.

Since the values of  $\{R_d^{\text{sim}}, r_0^{\text{sim}}, z^{\text{sim}}\}$  are directly obtained from the simulation outputs and thus are free from observational uncertainties, the likelihood for the  $i$ -th galaxy simplifies to

$$\begin{aligned} \mathcal{P}(\mathcal{D}_i | \Theta) &= \int \mathcal{P}(\mathcal{D}_i | \Phi_i) \mathcal{P}(\Phi_i | \Theta) d\Phi_i = \\ &= \int \delta(\mathcal{D}_i - \Phi_i) \mathcal{P}(\Phi_i | \Theta) d\Phi_i. \end{aligned} \quad (\text{B3})$$

The probability distribution describing the  $R_d$ - $r_0$  relation at a given redshift is modeled as a normal distribution,

$$\mathcal{P}(\Phi | \Theta) = \mathcal{N} \left( \log r_0 \mid \mu(z, \log R_d), \sigma^2(z) \right), \quad (\text{B4})$$

where  $\mu(z, \log R_d)$  is the mean relation defined in Equation 5, and  $\sigma(z)$  represents the intrinsic scatter of the population as in Equation 9.

**Table B1.** Settings adopted for the DYNESTY nested sampling run. Column 1 lists the parameters of the DynamicNestedSampler class and the run\_nested method. Column 2 reports the adopted values.

Parameter	Value
nlive	1000
dlogz_init	0.01
sampler	DynamicNestedSampler
rstate	numpy.random.default_rng(18)
ndim	len(param_labels)

**Table B2.** Prior ranges adopted for the hyperparameters of the evolutionary single power-law model.

Parameter	Description	Prior range
$\log r_{0,0}$	Normalization at $z = 0$	$\mathcal{U}(0.0, 1.5)$
$\log r_{0,z}$	Redshift dependence of normalization	$\mathcal{U}(-0.5, 0.5)$
$\alpha_0$	Slope at $z = 0$	$\mathcal{U}(0.5, 3.0)$
$\alpha_z$	Redshift dependence of slope	$\mathcal{U}(-0.5, 0.5)$
$\sigma_0$	Intrinsic scatter at $z = 0$	$\mathcal{U}(0.01, 0.50)$
$\sigma_z$	Redshift dependence of scatter	$\mathcal{U}(-0.2, 0.2)$

The posterior distributions of all hyperparameters

$$\Theta = \{\log r_{0,0}, \log r_{0,z}, \alpha_0, \alpha_z, \sigma_0, \sigma_z\},$$

are sampled using the nested sampling algorithm implemented in DYNESTY (Speagle 2020; Koposov et al. 2023), adopting the configuration summarized in Table B1. The sampler was initialized with a fixed random state to ensure reproducibility and run in dynamic mode, which adaptively allocates new live points during the exploration of the posterior volume. This technique efficiently explores multi-dimensional parameter spaces and provides both the full posterior and the Bayesian evidence. Table B2 lists the priors adopted for the model. The posterior distributions of all model parameters are shown in Figure B1. The contours highlight the covariance structure among the hyperparameters, with diagonal panels displaying the marginalized one-dimensional posterior probability density functions (PDFs). This hierarchical formalism allows us to self-consistently quantify the redshift evolution of both the slope and normalization of the  $R_d$ - $r_0$  relation, as well as the gradual tightening of its intrinsic scatter toward lower redshifts, consistent with the trends discussed in section 5.

This paper has been typeset from a  $\text{\LaTeX}$  file prepared by the author.

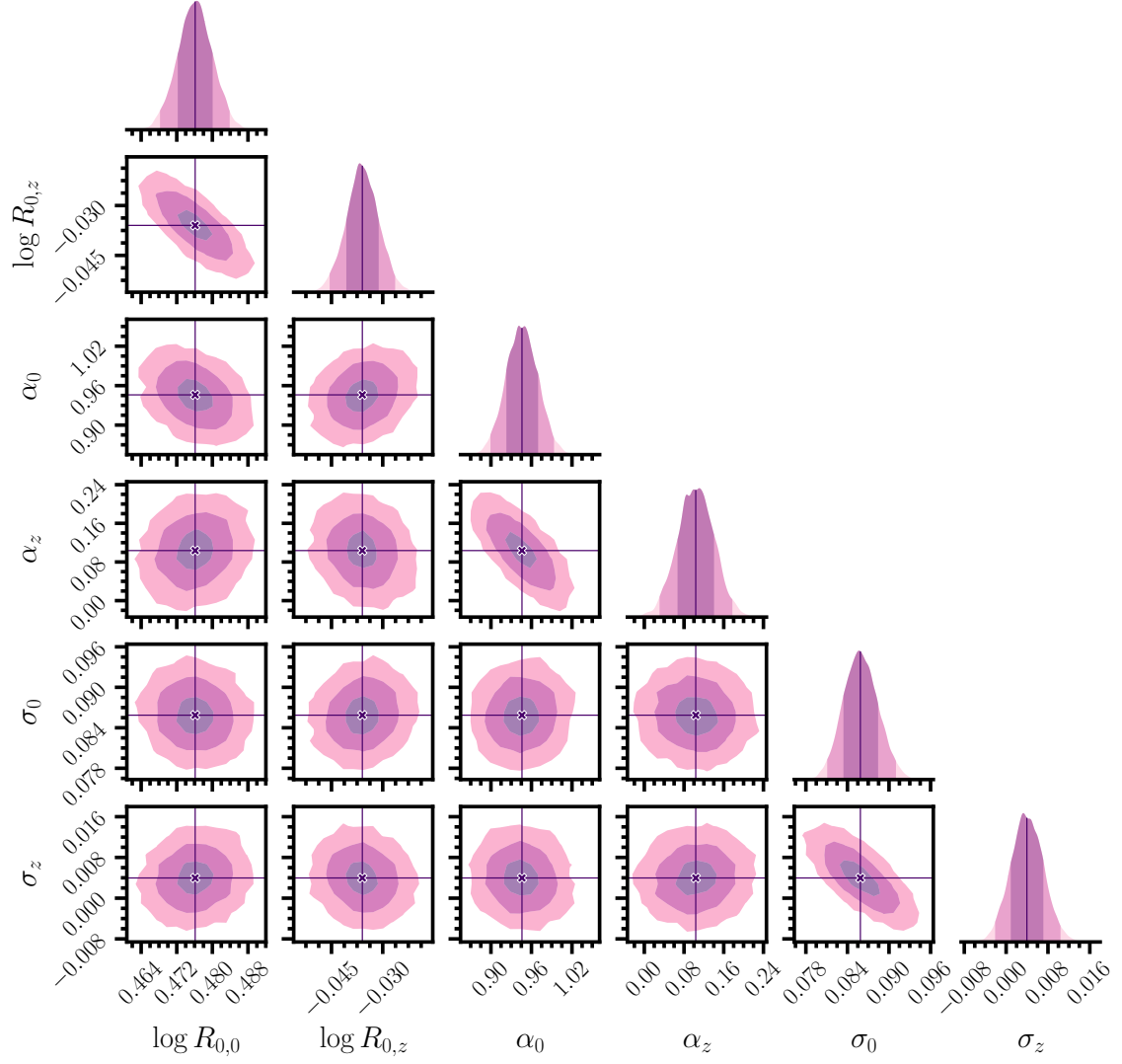


**Figure B1.** Posterior distributions of the model parameters describing the redshift evolution of the  $R_d-r_0$  relation. Diagonal panels show the marginalized one-dimensional probability density functions (PDFs), while off-diagonal panels display the two-dimensional joint posteriors with the 1, 2, and 3 $\sigma$  credible contours. The parameters include the normalization  $\log R_{0,0}$  and its redshift evolution term  $\log R_{0,z}$  of Equation 6, the slope  $\alpha_0$  and its evolution  $\alpha_z$  of Equation 7, and the intrinsic scatter  $\sigma_0$  and its evolution  $\sigma_z$  of Equation 9. Contours and shaded regions correspond to the 68%, 95%, and 99.7% confidence intervals derived from the nested sampling inference.